DUAL-PLANE STEREO PIV (DSPIV) MEASUREMENTS OF THE VELOCITY GRADIENT TENSOR FIELD AT THE SMALL SCALES OF TURBULENT FLOWS

John A. Mullin and Werner J.A. Dahm
Laboratory for Turbulence & Combustion (LTC)
Department of Aerospace Engineering
The University of Michigan
Ann Arbor, MI 48109-2140 USA

ABSTRACT

We present results from the first direct nonintrusive fully-resolved simultaneous measurements of the complete nine-component velocity gradient tensor field $\nabla \mathbf{u}(\mathbf{x},t)$ in a turbulent shear flow. The measurement technique involves a unique frequency-based dual-plane stereo PIV system that provides all three velocity components $u_i(\mathbf{x},t)$ in two differentially-spaced measurement planes formed by two pairs of double-pulsed light sheets, in this case at 532 nm and 635 nm. Tests using synthetic PIV, single-plane imaging and coincident-plane imaging allow assessments of the accuracy of such measurements. Direct differentiation of velocity components within each plane and between planes provides the full $\nabla \mathbf{u}(\mathbf{x},t)$ field in a plane, and thus the instantaneous spatial structure and statistics of gradient fields such as the true vorticity vector field $\omega(\mathbf{x},t)$, the full strain rate tensor field $\varepsilon(\mathbf{x},t)$, and the true kinetic energy dissipation rate field $2\nu\,\varepsilon{:}\varepsilon(\mathbf{x},t)$. Present results characterize the accuracy of these measurements, and provide initial examples of the resulting structure, statistics, and scalings of such gradient fields in turbulent shear flows.

INTRODUCTION

Experiments designed to measure the fully-resolved velocity gradient tensor field in turbulent flows provide data for subgrid-scale modeling studies at a resolution and detail that has previously been possible only by direct numerical simulations, but at Reynolds numbers and flow conditions far exceeding those accessible by DNS. Such measurements must provide all three components of velocity on multiple planes or in a volume, with full spatial and temporal resolution. Approaches such as PTV (*e.g.*, Kasagi & Nishino 1991, Malik *et al* 1993) and HPIV (*e.g.*, Zhang *et al* 1997, Meng 1999) provide multi-component velocity fields, but not with the resolution and accuracy needed to capture gradients fields at the small scales of turbulence. Kähler & Kompenhans (1999) and Hu *et al* (2001) used polarization-based dual-plane stereo PIV with two orthogonally polarized light sheets and polarization filters to separate the Mie scattering from spherical liquid droplets onto two pairs of stereo PIV cameras. The need for spherical droplets as the seed "particles" in such a polarization-based approach results from the requirement to preserve the polarization in the scattered light, so it can be separated via filters onto the individual camera pairs. This works in nonreacting flows, but in highly exothermic turbulent reacting flows of interest for combustion and propulsion, liquid droplets do not survive and polarization-based methods cannot be used. Yet in such flows measurements are needed to reveal the effects of exothermicity on the structure and scaling of velocity gradient quantities for subgrid model development.

Mullin & Dahm (2002) introduced the first frequency-based dual-plane stereo PIV (DSPIV) approach, in which two different laser frequencies are used in conjunction with filters to separate the light scattered from seed particles onto the individual camera pairs. This allows traditional solid metal oxide particles to be used as the seed, and thus permits measurements in reacting as well as nonreacting flows. In particular, this approach permits direct comparisons of reacting and nonreacting flows to reveal the effects of exothermicity at the diffusive scales of the flow, which are of key interest for subgrid modeling of reacting flows. This paper gives assessments of the frequency-based DSPIV method and initial results for velocity gradient fields.

FREQUENCY-BASED DSPIV MEASUREMENTS

The frequency-based DSPIV method is described in detail by Mullin & Dahm (2002, 2003). As shown in Fig. 1, we use two different frequencies of laser light in conjunction with
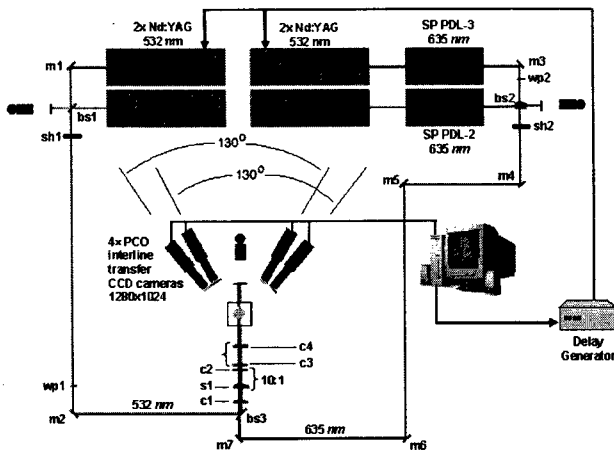
Figure 1. Basic arrangement for frequency-based dual-plane stereo PIV (DSPIV), providing measurements of all three velocity component fields in two differentially-spaced planes.

Figure 2. Direct differentiation of the u, v, and w-component fields within each plane (x,y) and between the two planes (z) provides the full velocity gradient tensor field $\nabla u(x,t)$.

the appropriate narrowband filters to separate the particle scattering onto the respective camera pairs. The present system is based on four frequency-doubled Nd:YAG lasers. Two are sequentially triggered to produce the double-pulsed 532 nm plane and the other two pump two dye lasers to produce the double-pulsed 635 nm plane as indicated in Fig. 2. Laser sheet thicknesses of 400 ± 20 μm are measured by a translating knife edge and photodiode. Differential sheet separation of 400 ± 20 μm and parallelism of ±0.01-deg are verified by direct imaging of targets at several locations over the field of view. Seeding is with 0.5 μm aluminum oxide particles. Two pairs of interline transfer CCD cameras in single-frame/double-exposure mode are positioned asymmetrically for forward scattering with angular displacements obeying the Scheimpflug condition. The cameras in each pair are respectively at 20° and 30° to

Velocity Component	Mean Velocity (m/s) 532 nm	635 nm	Percent Error 532 nm	635 nm
u	0.936	0.939	6.8	6.4
v	0.992	0.993	0.8	0.7
w	0.987	0.973	1.3	2.7

Table 1. Mean velocities and errors from green and red camera pairs for synthetic particle fields with uniform displacement and time delay corresponding to 1 m/s in each component.

Velocity Component	σ_i (m/s) 532 nm	σ_i (m/s) 635 nm	σ_i (m/s) 532 – 635
u	0.006	0.004	0.003
v	0.004	0.004	0.003
w	0.008	0.008	0.005
ER	1.79	2.00	

Table 2. Standard deviation of error in each velocity component from synthetic DSPIV calibrations in Table 1, giving error ratio for each of green and red stereo PIV arrangements.
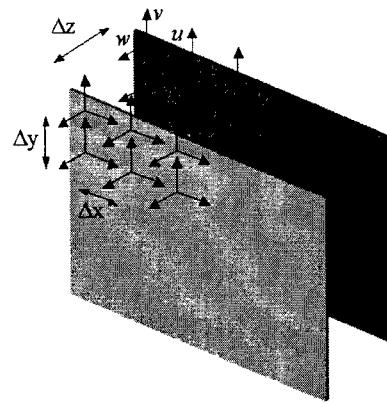
the light sheet normal; the 50° included angle for each pair is in accordance with optimal asymmetric system performance (Coudert *et al* 1999). Particle images are obtained with 300 mm macro lenses at 1:1.8 image ratio and span a 15 mm × 12 mm region in the flow. The resulting dynamic velocity range (DVR) of 31.4 and dynamic spatial resolution (DSR) of 38.5 allows resolution of velocities as small as 0.031 m/s with a 102 μs time delay, while still resolving the maximum velocities in the measurement region.

Particle images are processed by an FFT-based cross-correlation multipass algorithm with interrogation window size satisfying the 1/4-rule. Resulting velocity fields have in-plane spatial resolution of 400 μm based on the interrogation box size, pixel size, and magnification. The 400 μm center-to-center separation of the red and green laser sheets matches this in-plane resolution, providing 400 μm cubic interrogation boxes. Post-processing removes spurious vectors (≤ 5% of total vectors) and applies a 3 × 3 median filter. The resulting velocity fields are differentiated via central differences for in-plane derivatives and one-sided differencing for out-of-plane derivatives to yield the velocity gradient tensor field $\nabla u(x,t)$. In all cases, x denotes the coordinate along the mean streamwise velocity component u, with z is the direction normal to the two SPIV planes and w the out-of-plane velocity component.

ASSESSMENT OF MEASUREMENT ACCURACY

Quantitative assessments of measurement accuracy, based on *(i)* synthetic DSPIV measurements, *(ii)* coincident plane DSPIV measurements, and *(iii)* statistical tests of resulting velocity gradient components, are essential to establishing the validity of the resulting $\nabla u(x,t)$ fields.

Synthetic PIV Assessment

Accuracy is first checked with a synthetic particle field, consisting of 0.5 μm dots on a 35 mm film negative, translated with a three-axis micrometer stage having 1.5 μm dis-
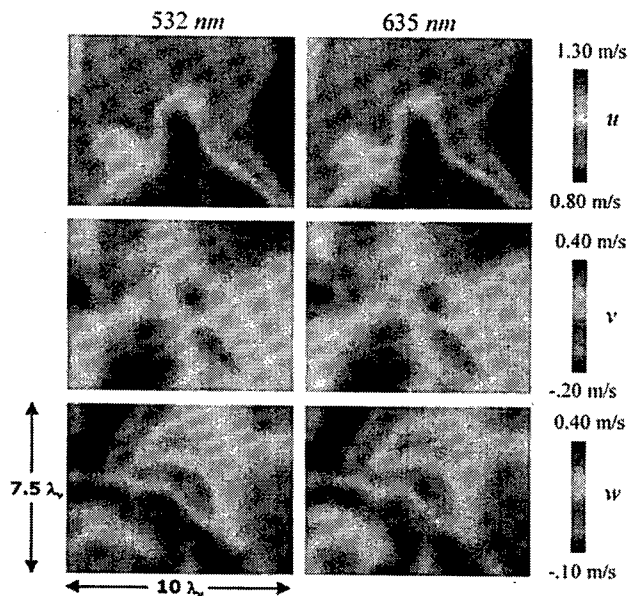
Figure 3. Typical velocity component fields from red and green camera pairs when both image the same laser sheets, providing quantitative assessment of velocity gradient accuracy.
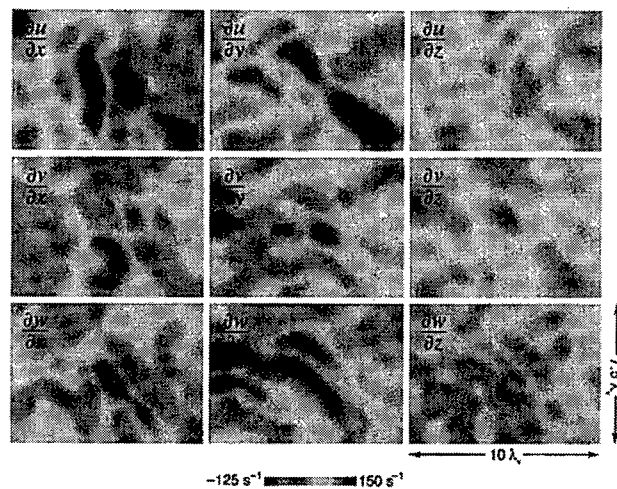

Figure 4. Velocity gradient components from Fig. 3; note z-derivatives are small relative to x- and y-derivatives, demonstrating negligible measurement differences between camera pairs.

placement uncertainty per axis. A 100 μm translation of this field in each direction reflects the maximum particle displacements expected between the two laser pulses for each SPIV plane. Tables 1 and 2 give the mean and rms of the resulting measured velocity components; the time delay corresponded to 1 m/s velocity in each component.

The errors in the mean values for the v and w components in Table 1 are consistent with the 1.5% micrometer position uncertainty per translation step in the synthetic particle displacements. The larger value in the u-component is from additional slip in the x-translation stage due to the weight of the calibration apparatus. The values in Table 2 are rms deviations from the mean velocity component values over the synthetic image, and represent bounds on the accuracy of the velocities resolvable by the imaging system and the DSPIV processing. The error ratio (ER) of about 2 for each camera pair is consistent with values reported by Lawson & Wu (1997) and Coudert $et\ al$ (1999) for such an asymmetric configuration. The last column shows that camera registration is not the main error source.

Single Plane Assessment

A second rigorous means to assess measurement accuracy is obtained by comparing velocity component fields from particle images in a turbulent flow when both camera pairs image a single plane; $i.e.$, the same pair of laser sheets. Differences in the velocity components from the two camera pairs then provide fundamental limits on the accuracy with which SPIV can measure velocities, and thus velocity gradients, for this asymmetric configuration

In this case, measurements were made on the centerline in the self-similar far field of an axisymmetric coflowing

turbulent jet at x/d = 100. The jet issued from a 2 mm tube into a 0.25 m/s uniform coflow. The mean velocity at the measurement location was $u \approx 0.98$ m/s. Aluminum oxide particles were seeded in both the jet and coflowing stream. The 15 $mm \times 12$ mm imaged region in the flow was much smaller than the local outer length scale $\delta(x) \approx 96$ mm of the jet, thus when normalized by the local inner variables v and λ_v (Buch & Dahm 1996, 1998) the resulting velocity gradient fields are reflective of the quasi-universal small scale structure of all turbulent shear flows at sufficient high outer-scale Reynolds number $Re_\delta \equiv u\delta/v$; the choice of a coflowing jet is then purely a matter of convenience for seeding purposes. In the present case, $Re_\delta \approx 6000$, giving the local inner (viscous) scale as $\lambda_v \approx 1600$ μm. The 400μm spatial resolution thus corresponds to $\lambda_v/4$, reflecting the highly resolved nature of these measurements.

Figure 3 shows a typical example of instantaneous velocity component fields obtained from the red and green camera pairs. Figure 4 provides the resulting velocity gradient component fields. Departures from zero z-derivative components reflect fundamental accuracy limits of the present asymmetric SPIV measurements. Note in Fig. 4 that z-

Velocity Component	σ_i (m/s) Single Plane	σ_i (m/s) Coincident Planes
u	0.011	0.021
v	0.013	0.017
w	0.022	0.034

Table 3. Standard deviation of velocity component differences from both camera pairs when imaging the same laser sheet, and when imaging coincident red-green laser sheets.
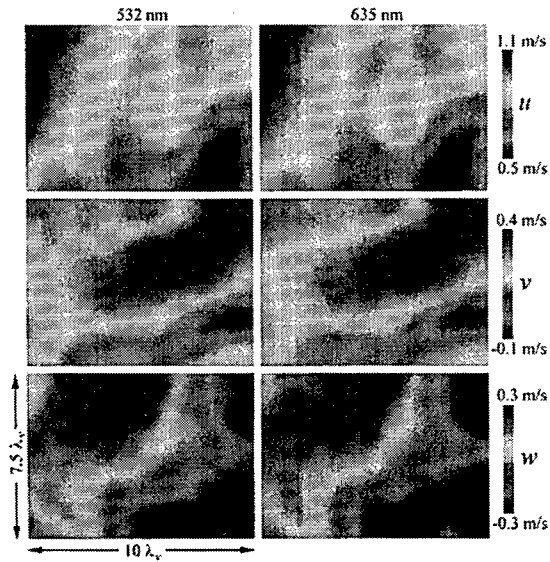
−283−

Figure 5. Typical velocity component fields obtained from each camera pair when red and green laser sheets are arranged to be coincident, allowing error assessment due to sheet positioning.

Figure 6. Velocity gradient components from Fig. 5. Slightly larger z-derivatives than in Fig. 4 quantify errors due to limits of red and green laser sheet positioning. See also Table 3.

derivative values are typically much smaller than x- and y-derivatives, with the largest errors occurring in $\partial w/\partial z$ due to the inherently larger w-errors in Table 2. Table 3 gives the resulting *rms* variation of the difference in each velocity component between the two camera pairs. Such limits apply to all DSPIV measurements, including the polarization approach.

Coincident Planes Assessment

Comparisons of the velocity component fields in a turbulent flow from the two independent camera pairs when the green and red sheets are arranged to be coincident ($\Delta z = 0$ in Fig. 2) provide a further rigorous means to assess additional errors due to laser sheet positioning. In this case, measurements were made in the same flow under identical conditions as above, but with camera pairs imaging separate red and green laser sheets arranged to be as nearly coin-
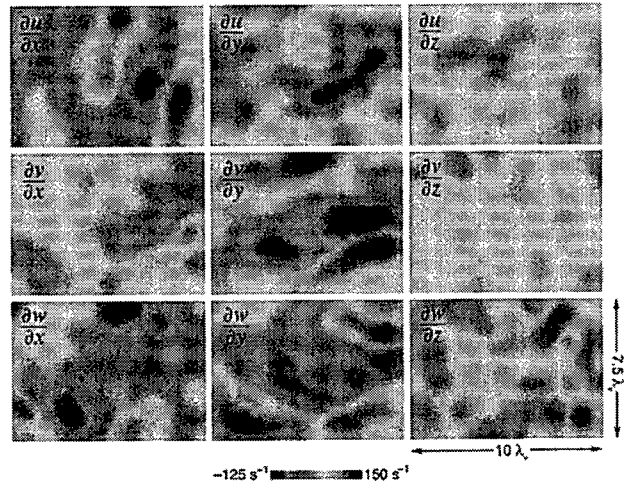
cident as possible with the present alignment system.

Figure 5 gives a typical example of the resulting instantaneous velocity component fields from the red and green camera pairs. Figure 6 shows the corresponding velocity gradient component fields. Departures from zero z-derivative components now reflect additional inaccuracy due to limits in sheet positioning. Note however that z-derivative magnitudes are essentially similar as in Fig. 4, verifying that laser sheet alignment is not the dominant error source.

Table 3 confirms that *rms* variations in the difference in each velocity component from the two camera pairs is only slightly larger for coincident planes than for the single-plane case. As a result, the dominant errors in these gradient fields are from fundamental limits inherent in SPIV measurement accuracy for the asymmetric configuration, rather than limitations in the ability to control thickness, position and parallelism of the red and green laser sheets.
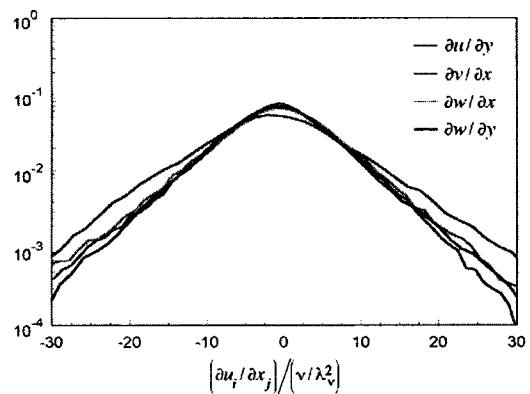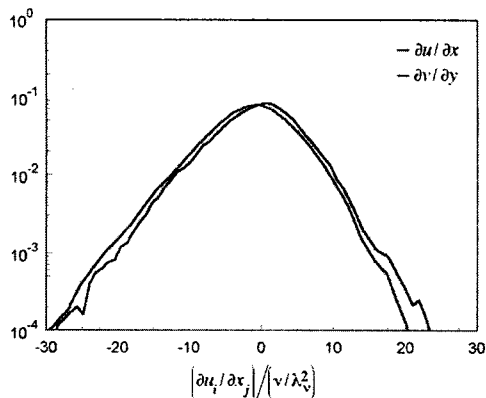

Figure 7. Probability densities of quasi-universal velocity gradient tensor components $\partial u_i/\partial x_j$ in turbulent shear flows, from DSPIV measurements with coincident planes. Results show good agreement of normal ($i = j$) components *(left)* and off-diagonal ($i \neq j$) components *(right)*, and resulting second moments accurately satisfy key isotropy relations. in (6)-(10).
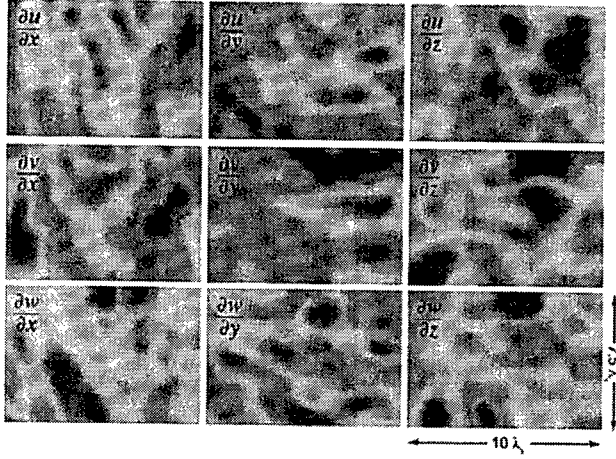
Figure 8. DSPIV-measured velocity gradient components on the inner scales of a turbulent shear flow. Dimensions are given in terms of the local inner (viscous) lengthscale.

Analysis of Derivative Uncertainties

Since the dominant errors in velocity differences were seen above to result from fundamental limits on the accuracy of SPIV measurements, these results allow uncertainty limits to be established for velocity gradient measurements. We can determine an upper bound for the relative error in each gradient component that ignores cancellation of individual velocity errors by the differencing process. Denoting

$$\delta_{u_i,x_j} \equiv \left(\sigma_i / \Delta x_j\right)/\left(\partial u_i/\partial x_j\right)_{rms} \tag{1}$$

and taking velocity fluctuations to be approximately homogeneous and isotropic, so that

$$\overline{\left(\frac{\partial u}{\partial x}\right)^2} \approx \frac{1}{15}\left(\frac{\varepsilon}{\nu}\right) \quad \text{and} \quad \overline{\left(\frac{\partial u}{\partial y}\right)^2} \approx \frac{2}{15}\left(\frac{\varepsilon}{\nu}\right), \tag{2a,b}$$

with

$$\left(\nu^3 / \varepsilon\right)^{1/4} \equiv \lambda_K \quad \text{and} \quad \lambda_K \approx 6\lambda_\nu, \tag{3a,b}$$

gives the error in the normal $(i = j)$ gradient components as

$$\delta_{u_i,x_j} \approx \frac{\sqrt{15}}{36}\left(\frac{\lambda_\nu^2}{\nu}\right)\left(\frac{\sigma_i}{\Delta x_j}\right), \tag{4}$$

with the coefficient for $i \neq j$ being one-half the value in (4). The σ_i's for the in-plane gradient components are the corresponding single-plane values in Table 3, and for out-of-plane components are the coincident plane values in the same table. Resulting derivative uncertainties are

$$\delta_{u_i,x_j} \approx \begin{pmatrix} 0.54 & 0.27 & 0.51 \\ 0.32 & 0.64 & 0.42 \\ 0.54 & 0.54 & 1.67 \end{pmatrix}. \tag{5}$$

These represent upper bounds for essentially any DSPIV (or SPIV) measurement of velocity derivatives. Actual errors may be much lower due to cancellation introduced by dif-

ferencing of velocities. Further reduction may be possible by increasing the separation between the two z-planes at the expense of reduced spatial resolution in the z-derivatives.

Velocity Gradient Validations

Velocity gradient components from the coincident plane measurements demonstrate characteristics that indicate significantly lower derivative inaccuracies than suggested by the error estimates in (5). Figure 7 shows probability densities for each of the six nonzero components from a total of 678 coincident DSPIV planes. The two normal components $(i = j)$ agree well, as do the four off-diagonal $(i \neq j)$ components, as would be required by isotropy. Asymmetry in the normal components, and exponential tails evident in the semi-logarithmic axes, further indicate that large values in the measured derivative fields do not result from random errors, and are instead consistent with established characteristics of gradient fields in turbulent flows.

Further quantitative validations are possible from (2a,b), which suggest that relative magnitudes of the measured gradient components should at least approximately satisfy

$$\overline{\left(\frac{\partial u_i}{\partial x_j}\right)^2} = \begin{pmatrix} 1 & 2 & 2 \\ 2 & 1 & 2 \\ 2 & 2 & 1 \end{pmatrix} \cdot \left(\frac{\varepsilon}{15\nu}\right). \tag{6}$$

The distributions in Fig. 7 allow various such isotropy constructs to be formed to check the validity of the measured gradients against these relations. For example, for the two leftmost columns in (6), which do not involve z-derivatives, the measured gradients give

$$\frac{\overline{\left(\frac{\partial u_i}{\partial x_j}\right)^2}}{\frac{1}{2}\left[\overline{\left(\frac{\partial u}{\partial x}\right)^2}+\overline{\left(\frac{\partial v}{\partial y}\right)^2}\right]} = \begin{pmatrix} 1.0 & 1.7 \\ 2.3 & 1.1 \\ 2.0 & 1.9 \end{pmatrix} \tag{7}$$

which are in reasonable agreement with (6). The measured velocity gradients also produce values of

$$\frac{\overline{\left(\frac{\partial u}{\partial y}\right)^2}+\overline{\left(\frac{\partial v}{\partial x}\right)^2}}{\overline{\left(\frac{\partial u}{\partial x}\right)^2}+\overline{\left(\frac{\partial v}{\partial y}\right)^2}} = 1.90 \quad \text{and} \quad \frac{\overline{\left(\frac{\partial w}{\partial x}\right)^2}}{\overline{\left(\frac{\partial w}{\partial y}\right)^2}} = 1.05 \tag{8, 9}$$

versus ideal isotropic values of 2 and 1, respectively, and

$$\frac{\left[\overline{\left(\frac{\partial w}{\partial x}\right)^2}+\overline{\left(\frac{\partial w}{\partial y}\right)^2}\right]}{\left[\overline{\left(\frac{\partial u}{\partial x}\right)^2}+\overline{\left(\frac{\partial u}{\partial y}\right)^2}+\overline{\left(\frac{\partial v}{\partial x}\right)^2}+\overline{\left(\frac{\partial v}{\partial y}\right)^2}\right]} = 0.64 \tag{10}$$

versus the ideal isotropic value of 2/3. All of these assessments suggest significantly higher validity in the meas-
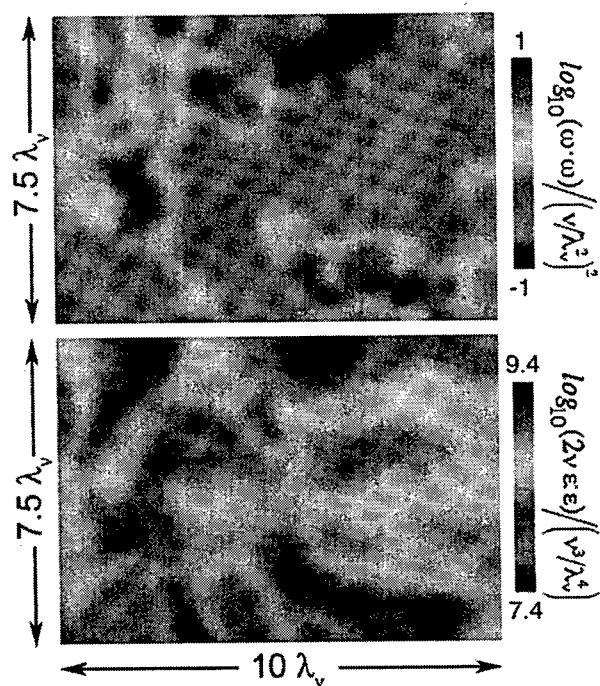
Figure 9. Enstrophy field *(top)* and kinetic energy dissipation rate field *(bottom)* from DSPIV measurements of velocity gradient fields in Fig. 8, shown with logarithmic color scale.

show agreement with isotropy statistics that indicate far higher accuracy in the gradient components than suggested by these bounds. Such measurements allow access to key gradient fields of interest for subgrid scale modeling in turbulent flows at conditions that are unattainable by DNS.

ured gradient fields, even in the w-components, than might be suggested by the upper bounds in (5).

MEASURED VELOCITY GRADIENT FIELDS

Having quantified the origins and relative magnitudes of uncertainties in such measurements, Fig. 8 presents typical results for all nine components of the velocity gradients at the inner scales of the turbulent shear flow noted above, but now with 400 μm separation between the green and red planes. Typical results for key turbulence fields of interest for subgrid scale modeling, including the corresponding true enstrophy field $\omega \cdot \omega(x,t)$ and the true kinetic energy dissipation rate field $2\nu \, \varepsilon{:}\varepsilon(x,t)$, are shown in Fig. 9.

CONCLUSIONS

The present results characterize the performance of a unique frequency-based dual-plane stereo PIV system for measuring the velocity field $u(x,t)$ in two differentially-spaced planes formed by two pairs of double-pulsed light sheets. Synthetic PIV as well as single- and coincident-plane imaging in a turbulent flow provide quantitative assessments for the accuracy of the underlying velocity measurements. Upper bounds on the individual gradient component uncertainties have been obtained, assuming no correlation of velocity errors between adjacent vectors and thus no error cancellation due to differencing. Actual measurements

REFERENCES

Buch, K.A. & Dahm, W.J.A. (1996) Experimental study of the fine-scale structure of conserved scalar mixing in turbulent shear flows. Part 1. $Sc \gg 1$. *JFM* **317**, 21-71.

Buch, K.A. & Dahm, W.J.A. (1998) Experimental study of the fine-scale structure of conserved scalar mixing in turbulent flows. Part 2. $Sc \approx 1$. *JFM* **364**, 1-29.

Coudert, S., Westerweel, J. & Fournel, T. (1999) Comparison between asymmetric and symmetric stereoscopic DPIV system. Proc. 10th Annual Symp. on Laser Techniques Applied to Fluid Mechanics., Lisbon, Portugal.

Hu, H., Saga, T., Kobayashi, T., Taniguchi, N. & Yasuki, M. (2001) Dual-plane stereoscopic particle image velocimetry system set-up and its application on a lobed jet mixing flow. *Expts. Fluids* **31**, 277-293.

Kähler, C.J. & Kompenhans, J. (1999) Multiple plane stereo PIV: technical realization and fluid-mechanical significance. *Proc. 3rd International Workshop on PIV*, Santa Barbara, U.S.A.

Kasagi, N., & Nishino, K. (1991) Probing turbulence with three-dimensional particle tracking velocimetry. *Experimental Thermal and Fluid Science* **4**, 601-613.

Lawson, N.J. & Wu, J. (1997) Three dimensional particle image velocimetry: experimental error analysis of a digital angular stereoscopic system. *Meas. Sci. Technol.* **8**, 1455- 1464.

Malik, N., Dracos, T., Papantoniou, D. (1993) Particle tracking in three-dimensional turbulent flows - Part II: Particle tracking. *Expts. Fluids* **15**, 279-294.

Meng, H. (1999) Tackling turbulence with holographic particle image velocimetry (HPIV). *AIAA Paper No.* 99-3755, AIAA, Washington D.C.

Mullin, J.A. & Dahm, W.J.A. (2002) Highly-resolved three-dimensional velocity measurements via dual-plane stereo particle image velocimetry (DSPIV) in turbulent flows. *AIAA Paper No.* 2002-0290, AIAA, Washington D.C.

Mullin, J.A. & Dahm, W.J.A. (2003) Fully-resolved DSPIV velocity field measurements at the quasi-universal scales of turbulence. *AIAA Paper No.* 2003-4150, AIAA, Washington D.C.

Zhang, J., Tao, B. & Katz, J. (1997) Turbulent flow measurement in a square duct with hybrid holographic PIV. *Expts. Fluids* **23**, 373-381.